Utilizing a NaOH Promoter to Achieve Large Single-Domain Monolayer WS$_2$ Films via Modified Chemical Vapor Deposition

Changyong Lan,[†,‡] Xiaolin Kang,[‡,§] Renjie Wei,[‡,§] You Meng,[‡,§] SenPo Yip,[‡,§,∥] Heng Zhang,[‡,§] and Johnny C. Ho*,[‡,§,∥]

†School of Optoelectronic Science and Engineering, University of Electronic Science and Technology of China, Chengdu 610054, China
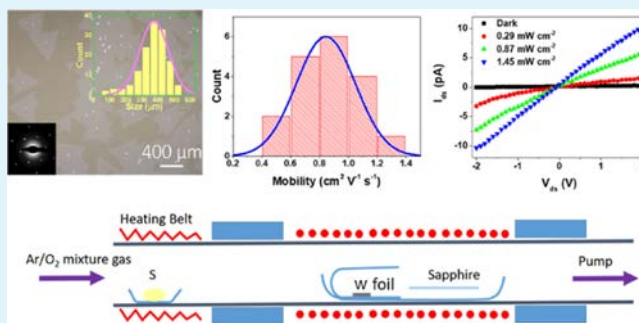
‡Department of Materials Science and Engineering and §State Key Laboratory of Terahertz and Millimeter Waves, City University of Hong Kong, Kowloon 999077, Hong Kong

∥Shenzhen Research Institute, City University of Hong Kong, Shenzhen 518057, China

Ⓢ *Supporting Information*

ABSTRACT: Because of their fascinating properties, two-dimensional (2D) nanomaterials have attracted a lot of attention for developing next-generation electronics and optoelectronics. However, there is still a lack of cost-effective, highly reproducible, and controllable synthesis methods for developing high-quality semiconducting 2D monolayers with a sufficiently large single-domain size. Here, utilizing a NaOH promoter and W foils as the W source, we have successfully achieved the fabrication of ultralarge single-domain monolayer WS$_2$ films via a modified chemical vapor deposition method. With the proper introduction of a NaOH promoter, the single-domain size of monolayer WS$_2$ can be increased to 550 μm, while the WS$_2$ flakes can be well controlled by simply varying the growth duration and oxygen concentration in the carrier gas. Importantly, when they are fabricated into global backgated transistors, WS$_2$ devices exhibit respectable peak electron mobility up to 1.21 cm^2 V^{-1} s^{-1}, which is comparable to those of many state-of-the-art WS$_2$ transistors. Photodetectors based on these single-domain WS$_2$ monolayers give an impressive photodetection performance with a maximum responsivity of 3.2 mA W^{-1}. All these findings do not only provide a cost-effective platform for the synthesis of high-quality large single-domain 2D nanomaterials, but also facilitate their excellent intrinsic material properties for the next-generation electronic and optoelectronic devices.

KEYWORDS: WS$_2$, chemical vapor deposition, NaOH promoter, transistor, photodetector

INTRODUCTION

Since the discovery of graphene, two-dimensional (2D) nanomaterials have attracted a great deal of attention in research and industry because of their fascinating chemical and physical properties.[1−3] In particular, semiconducting 2D nanomaterials are demonstrated to have great potential for applications in next-generation electronics and optoelectronics.[3−5] For instance, WS$_2$ is an exciting kind of semiconducting 2D nanomaterial, which exhibits many novel phenomena, such as the layer-dependent band gap and band structure, high photoluminescence (PL) quantum yield, large exciton binding energy, valley-dependent transition selection rule, and so forth.[6] These unique characteristics would make WS$_2$ an ideal active device material for high-performance transistors, photodetectors, light-emitting devices, and many others.[7−9]

However, synthesis of high-quality 2D nanomaterials (including monolayer WS$_2$) with a large single-domain size is quite challenging, which substantially restricts their deploy-

ment for practical uses.[10] Typically, chemical vapor deposition (CVD) is always employed for the growth of wafer-scale 2D nanomaterials.[11] Until now, wafer-scale fabrication of several 2D nanomaterials (e.g. graphene, MoS$_2$, and WS$_2$) has been readily developed with various CVD methods,[8,12,13] but the crystal quality of most obtained materials is poor, as they are composed of relatively small grains with high defect concentration.[8,12,13] Inevitably, when they are fabricated into devices, these nanomaterials always give degraded performance as compared to the ones made from their mechanically exfoliated counterparts. In this case, synthesizing large single-domain 2D nanomaterials becomes urgently desired for technological utilizations. Different modified CVD methods have then been explored to achieve high-quality large single-domain 2D transition-metal dichalcognides (TMDCs) during
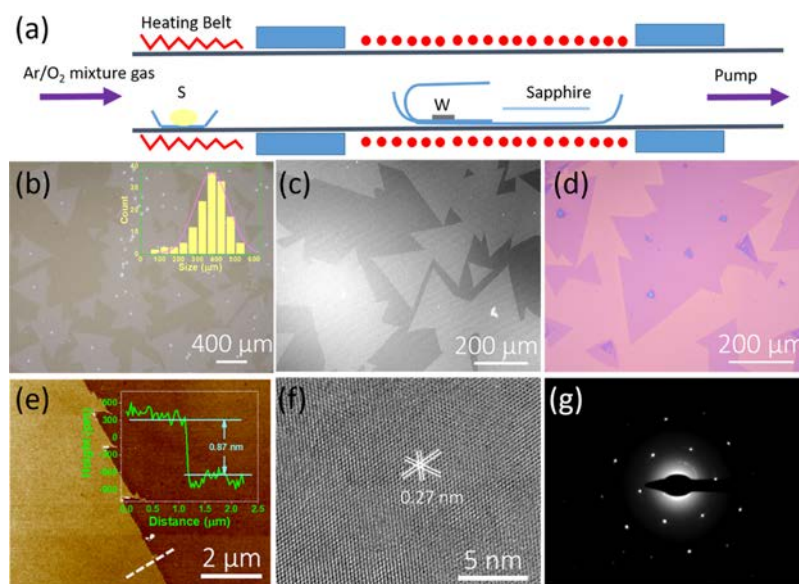
Figure 1. Schematic of the growth setup and characterization of the obtained WS$_2$. (a) Schematic setup for the synthesis of WS$_2$. (b) OM image of WS$_2$ on sapphire. Inset: Size distribution of the WS$_2$ flakes. (c) SEM image. (d) OM image of WS$_2$ transferred on SiO$_2$ (270 nm)/Si. (e) AFM image. Inset: Height profile along the white dashed line. (f) HRTEM image. (g) SAED pattern. The growth duration and oxygen concentration (in volume ratio) for the WS$_2$ flakes shown here are 30 min and 1.0%.

the past few years. It is possible to enlarge the single-domain size by accelerating the lateral growth. Under a high sulfur/WO$_3$ ratio, Xu et al. found that the dominating growth is the lateral growth when synthesizing WS$_2$ monolayer flakes by an atmospheric pressure CVD method on sapphire.[14] As a result, large WS$_2$ monolayer flakes of about 135 μm could be obtained. Substrate treatment is another way toward the large single-domain TMDCs. Chen et al. found that high-quality WS$_2$ films with single domains of approximately tens or even hundreds of micrometers could be obtained by silanization treatment of Si substrates.[15] The silanization treatment of the Si substrate led to the uniform dispersion of WO$_3$ precursors, which is beneficial for the subsequent formation of high-quality WS$_2$ during the CVD process. Recently, it was observed that controlling the nucleation density is a versatile method for the synthesis of large single-domain TMDCs. In order to control the nucleation density of TMDCs, various methods were tried. Yue et al. found that the nucleation density could be effectively controlled by adjusting the introduction time of S precursors and the distances between the W source and the substrate.[16] Thus, monolayer WS$_2$ flakes as large as 233 μm could be obtained. Because Au can reduce the barrier energy for the sulphurization of WO$_3$ by S atoms, a much lower concentration of WO$_3$ and S could sustain the growth of WS$_2$ on Au with a low nucleation density.[17] This way, Gao et al. could synthesize monolayer WS$_2$ films with the size of single domains approaching 1 mm on Au substrates.[17] Yang et al. found that Na in the soda-line glass could act as catalysts to promote the growth of MoS$_2$.[18] They used Mo foil as the Mo source and adopted a face-to-face configuration to the soda-line glass substrate. The nucleation density could then be well controlled by the distance between the Mo foil and the soda-line glass. Therefore, they could synthesize large single-domain MoS$_2$ monolayer flakes up to 400 μm. These investigations suggest the importance of controlling the nucleation density in realizing large 2D TMDC flakes during CVD synthesis. In this regard, new methods for controlling the nucleation density is

highly desired for the growth of large single-domain 2D materials.

In this work, utilizing a NaOH promoter and W foils as the W source, the nucleation density can be well controlled by tuning the growth parameters, and we successfully achieved the synthesis of ultralarge single-domain monolayer WS$_2$ films via the modified CVD method. With the introduction of a NaOH promoter, the single-domain size of monolayer WS$_2$ can be increased to 550 μm, while the WS$_2$ flakes can be well controlled by simply varying the growth duration and oxygen concentration in the carrier gas. When configured into backgated transistors, the WS$_2$ devices exhibit a peak electron mobility of 1.21 cm^2 V^{-1} s^{-1}. Photodetectors based on these large single-domain monolayer WS$_2$ also yield the respectable performance with a maximum responsivity of 3.2 mA W^{-1}. All these results can not only provide new insights into the synthesis of large single-domain size of 2D nanomaterials but also facilitate their applications in next-generation electronics and optoelectronics.

■ EXPERIMENTAL SECTION

Synthesis of Monolayer WS$_2$. For the synthesis of monolayer WS$_2$ flakes, W foil pieces (99.99%, 5 × 10 mm^2) with a thickness of 0.1 mm was used as the W source. The W foil was first dipped in 1 M NaOH solution for 5 min and then dried in air naturally. Next, the W foil was placed in the inner side of a quartz cuvette with a length of 4 cm. The quartz cuvette was subsequently transferred onto a quartz boat. A piece of single side polished sapphire was placed adjacent to the open end of the quartz cuvette in the quartz boat. The quartz boat was eventually inserted into the center of a quartz tube, which was mounted into a horizontal tube furnace. S powder was placed in a corundum boat, which was placed at the upstream of the quartz tube. To start the growth, the pressure within the quartz tube was pumped to a base pressure of 1 mTorr. A mixture gas of Ar and O$_2$ with a flow rate of 100 sccm was introduced into the quartz tube, while the pressure would be stabilized at 0.35 Torr. After that, the furnace was raised to 950 °C in 30 min and kept at that temperature for a duration of 10−40 min. S powder was heated by a heating belt with a

temperature of 140 °C. After the synthesis, the color of the sapphire substrate became light yellow.

Characterization. The optical microscopy (OM) images were recorded using an Olympus BX53 optical microscope with reflected illumination. The morphology of the WS$_2$ flakes was evaluated by a scanning electron microscope (G2 Pro, PhenomWorld). An atomic force microscope (diMultiMode V, Veeco) was used to measure the morphology and the thickness of the WS$_2$ flakes. The crystallinity of the WS$_2$ was assessed by a transmission electron microscope (JEOL 2100F, JEOL Co., Ltd.) after transferring the WS$_2$ flakes onto the transmission electron microscopy (TEM) grids. A Raman spectroscope (SR-5001-A-R, Andor) with a 532 nm excitation laser was employed to obtain the Raman and PL spectra of WS$_2$. An X-ray photoelectron spectroscope (ULVAC-PHI5802) was used to acquire the X-ray photoelectron spectroscopy (XPS) spectra of WS$_2$.

Device Fabrication and Measurement. For device fabrication, the WS$_2$ flakes were first transferred from sapphire substrates to SiO$_2$ (270 nm)/Si substrates by a surface energy-assisted method.[19] After the transfer of WS$_2$ onto SiO$_2$/Si, the standard photolithography method was used to define the source and the drain regions. Then, 5 nm Ti and 50 nm Au were deposited onto the substrate successively by e-beam evaporation followed by a lift-off process. The electrical performance of fabricated field-effect transistors was measured in a vacuum probe station. The chamber was pumped down to 4×10^{-4} Pa before measurement. An Agilent B1500A semiconductor analyzer was used as the source and measurement units. For the measurement of fabricated photodetectors, a 532 nm laser was used as the light source, which was introduced to the vacuum chamber by an optical fiber with a collimator at the end. The light intensity was tuned by an attenuator and measured by a power meter (PM400, Thorlabs). A home-made mechanical chopper combined with a signal generator was used to modulate the light.

■ RESULTS AND DISCUSSION

As depicted in the growth schematic in Figure 1a, a piece of W foil predipped in 1 M NaOH is used as the W source, which is placed in a semi-sealed quartz tube. With this special setup, the single-domain size of monolayer WS$_2$ as large as 550 μm can be obtained (Figure 1b), while the lateral size of these triangular-shaped WS$_2$ sheets follows Gaussian distribution with an average size of 375 μm (Figure 1b inset). This domain size is comparable with the ones synthesized using Au foil substrates and larger than most of the values reported in the literature as listed in Table 1. This impressively large single-domain size of WS$_2$ sheets is also confirmed by scanning electron microscopy (SEM) as shown in Figure 1c. After the transfer of WS$_2$ from sapphire to SiO$_2$ (270 nm)/Si, the triangular features of WS$_2$ flakes can be more clearly observed (Figure 1d). It should be noticed that the center of most of the WS$_2$ sheets has a thick layer area, which may be the nucleation

center during the growth. In order to get the precise thickness of the WS$_2$ sheets, atomic force microscopy (AFM) measurements are carried out. The typical AFM image is shown in Figure 1e. From the height profile along the white dash line (Figure 1e inset), the thickness of the WS$_2$ flakes is about 0.87 nm, which is consistent with the thickness of single-layer WS$_2$,[20] indicating that the large triangle sheets are single layer WS$_2$. Interestingly, these triangular sheets do not come with the perfectly straight and sharp edges but rather have the saw-tooth-like morphology, which is evidently observed in the corresponding high-resolution SEM image (Supporting Information Figure S1). The origin of these saw-tooth-like edges may be attributed to the competition between the atom adsorption rate and the edge diffusion rate during the material synthesis.[21] For evaluating the crystallinity of obtained WS$_2$ sheets, TEM measurements are performed. As shown in the typical high-resolution TEM (HRTEM) image in Figure 1f, clear lattice fringes are observed, indicating the good crystallinity of WS$_2$. Lattice spacings of 0.27 nm are identified, which can be ascribed to the {110} planes of WS$_2$. The selected area electron diffraction (SAED) pattern of a single WS$_2$ sheet is also collected with clear and sharp diffraction spots (Figure 1g), further confirming the excellent crystallinity of WS$_2$ being consistent with the HRTEM result discussed above. All these findings demonstrate that the high-quality and large single-domain monolayer WS$_2$ can be effectively achieved via the modified CVD method using a NaOH promoter. In addition, it should be noticed that the WS$_2$ monolayer flakes have the similar alignment. In order to evaluate the relative orientation of the WS$_2$ flakes to the sapphire substrate, the intersection angles of the triangle WS$_2$ flakes with the horizontal line in Figure 1b were measured and are shown in Supporting Information Figure S2. The WS$_2$ flakes show preferential angles at 24° and 84°, indicating the epitaxial relationship with the underlying sapphire substrate. The van der Waals epitaxial relation has also been observed in CVD grown MoS$_2$ on sapphire substrates.[22−24] The epitaxial growth is caused by the similar lattice symmetry of WS$_2$/MoS$_2$ and perfect lattice registry with sapphire.[22,24] Because of the weak van der Waals epitaxial confinement,[24] many unaligned WS$_2$ flakes can as well be observed (Supporting Information Figure S2).

In order to further evaluate of the crystal quality of obtained WS$_2$ sheets, Raman spectra of WS$_2$ are measured. As depicted in Figure 2a, several characteristic Raman peaks of WS$_2$ are clearly observed, where the peak centered at 299.5 cm^{-1} can be assigned to the $2LA(M) - 2E^2_{2g}(\Gamma)$ mode and the peak centered at 327.7 cm^{-1} can be attributed to the $2LA(M) - E^2_{2g}(\Gamma)$ mode. The peaks near 350 cm^{-1} can be resolved into three peaks located at 344.1, 353.9, and 358.1 cm^{-1}, belonging to the $E^1_{2g}(M)$, $2LA(M)$, and $E^1_{2g}(\Gamma)$ modes, respectively, while the peak centered at 417.8 cm^{-1} is ascribed to the A_{1g} mode. Notably, the wavenumber difference of between $E^1_{2g}(\Gamma)$ and $A_{1g}(\Gamma)$ is 59.7 cm^{-1}, together with the absence of the peak near 310 cm^{-1}, indicating that the obtained WS$_2$ is a single layer,[27,32] which is consistent with the AFM result (Figure 1e). Furthermore, as monolayer WS$_2$ is a direct band gap semiconductor, it always gives a strong PL.[33] The typical PL spectrum of WS$_2$ is displayed in Figure 2b. There is a strong emission near 1.96 eV observed, which belongs to the excitonic emission of monolayer WS$_2$.[27] It should be noticed that this emission peak contains a combination of multiple peaks because the profile does not exhibit a single Gaussian-like

Table 1. Lateral Size of Monolayer WS$_2$ Single Domains

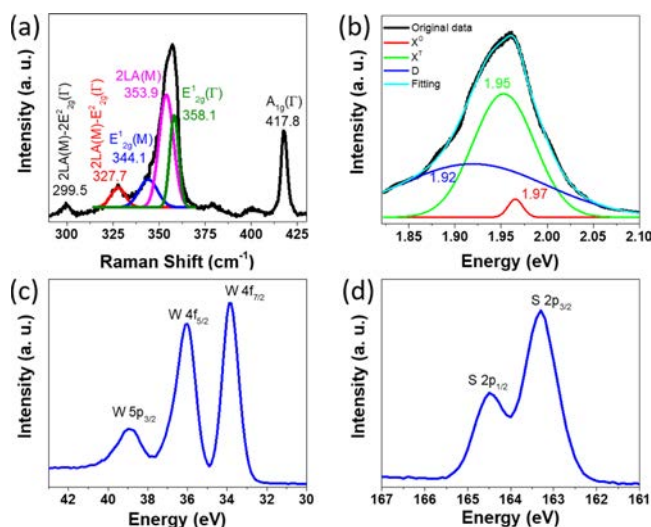| W source	substrate	lateral size (μm)	electron mobility (cm^2 V^{-1} s^{-1})	refs
W foil	sapphire	the largest: 550, average: 375	0.43−1.21	our work
WO$_3$	Au foil	800	1−2	17
WO$_3$	Au foil	420	20	25
WO$_3$	sapphire	∼30	0.46	20
WO$_3$	SiO$_2$/Si	200−350		26
WO$_3$	SiO$_2$/Si	the largest: 178		27
WO$_3$	SiO$_2$/Si	150	0.53	28
WO$_3$	SiO$_2$/Si	200	1.4	29
WO$_3$	SiO$_2$/Si	the largest: 320		30
H$_2$WO$_4$	SiO$_2$/Si	100	28	31

Figure 2. Spectroscopic characterization of the monolayer WS$_2$. (a) Raman spectrum of WS$_2$. (b) PL spectrum of WS$_2$. The curve is fitted by Gaussian function. X^O, X^T, and D denote the contribution from neutral exciton, charged exciton, and defect-related emission, respectively. (c) XPS spectrum of W. (d) XPS spectrum of S.

Figure 3. Characterization of W foils. (a) SEM image of a typical W foil. (b) SEM image of a W foil predipped with NaOH. (c) XRD pattern of the W foil before and after processing. W: unprocessed W foil without any treatment other than thorough cleaning, W−Na: W foil predipped in NaOH, W−S: W foil reacted with S, W−Na−S: W foil predipped in NaOH and then reacted with S.

curve. Gaussian fitting is then used to identify the peak positions of these multiple peaks near 1.96 eV, whereas three distinct peaks located at 1.92, 1.95, and 1.97 eV are resulted. Based on the literature report, these three peaks come from the defect-related emission (D), charged exciton (X^T), and neutral exciton (X^O) of monolayer WS$_2$, respectively.[34] The existence of defect-related emission suggests that there are some lattice defects existing in the WS$_2$ sheets. At the same time, the chemical composition and valence state of WS$_2$ sheets can be assessed by XPS. There are three characteristic peaks associated with W 5p$_{3/2}$, W 4f$_{5/2}$, and W 4f$_{7/2}$ for the scan of W species (Figure 2c), while there are two distinct peaks related to S 2p$_{1/2}$ and S 2p$_{3/2}$ observed for the scan of S species (Figure 2d). These results further confirm the successful synthesis of high-quality monolayer WS$_2$ investigated here.

With the aim of controlled synthesis, it is important to thoroughly understand the growth mechanism of large single-domain WS$_2$ using this modified CVD method. It is evident that the introduction of NaOH and the employment of W foil are key for the synthesis of monolayer WS$_2$ here. Without predipping the W foil in NaOH solution, there are almost no WS$_2$ flakes obtained under the same synthesis condition. This result indicates that NaOH is beneficial for the formation of W-contained vapor species. In order to investigate what has happened to the W foil during the dipping process, SEM images of the W foil before and after NaOH dipping are collected and given in Figure 3a,b, respectively. It can be seen that the as-obtained W foil has the relatively flat surface but the surface becomes rougher after NaOH dipping. As shown in the X-ray diffraction (XRD) pattern in Figure 3c, there are some amounts of WO$_3$ existed on all W foils. Possible reactions between WO$_3$ and NaOH can then happen, leading to the formation of Na$_2$WO$_3$ together with the rough surface for the W foil predipped with NaOH. Also, some NaOH would remain on the W foil surface and we intentionally do not wash it away. In any case, because of the strong diffraction signals from W, these materials cannot be directly observed from the XRD pattern. In fact, when the washed W foil is used as the W source, the obtained result is found to be the same as using the
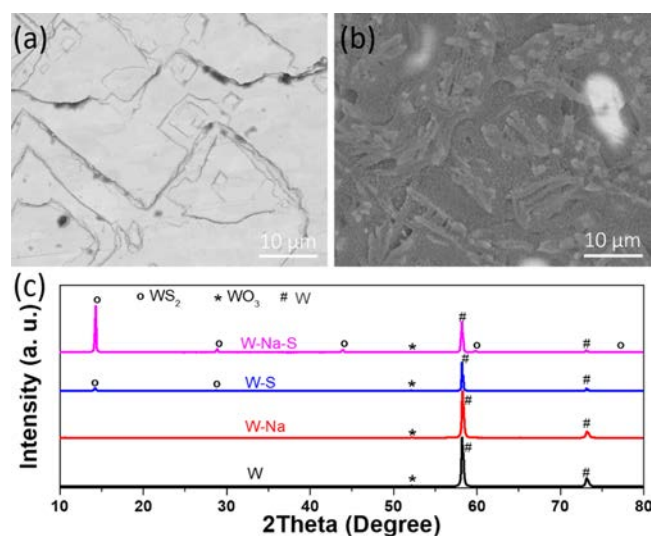
unprocessed W foil, indicating the important role of NaOH during the synthesis. After the synthesis of WS$_2$, the XRD spectrum of the W foil is also evaluated (Figure 3c). For the foil predipped with NaOH, the peak intensity of WS$_2$ is much stronger than the undipped one. For the undipped one, both S and O$_2$ would react with the W foil. As there is a large amount of S species, dense WS$_2$ film will form on the surface of W foil (Supporting Information Figure S3a). Inevitably, this dense WS$_2$ layer subsequently prevents the continuous sulfurization of the W foil, which leads to the weak diffraction peaks of WS$_2$ (Figure 3c). As a result, almost no WO$_x$ or WS$_2$ species can be transported to the sapphire substrate. This way, it is impossible for the growth of WS$_2$ onto the sapphire substrate under this condition. For the dipped foil, the diffraction peaks of WS$_2$ is very strong, which infers that much of the W foil is sulfurized into WS$_2$. The possible reaction during the synthesis can be depicted as the following

$$\text{NaOH} + \text{W} + \text{O}_2 \rightarrow \text{Na}_2\text{WO}_3 + \text{H}_2\text{O} \tag{1}$$

and

$$\text{Na}_2\text{WO}_3 + \text{S} \rightarrow \text{Na}_2\text{O} + \text{WS}_2 \tag{2}$$

In this case, it is anticipated that Na$_2$WO$_3$ is more volatile as compared to WO$_3$, which can be transported to downstream easily and then reacted with S, forming WS$_2$ on the substrate. As a result, the formation rate of Na$_2$WO$_3$ is a crucial parameter in controlling the synthesis of high-quality WS$_2$. Because of the consumption of W species, the surface of the W foil after the reaction becomes porous (Supporting Information Figure S3b). It has also been reported that Na species can act as a very effective promoter for the growth of MoS$_2$ because Na species reduce the barrier for the formation of MoS$_2$.[18] Because of the similarity of WS$_2$ with MoS$_2$, Na species are also anticipated to act as a promoter for the growth of large single-domain WS$_2$ monolayer flakes.

Apart from NaOH, it is found that the oxygen concentration of the growth environment also has a significant effect in controlling the domain size of monolayer WS$_2$. To shed light
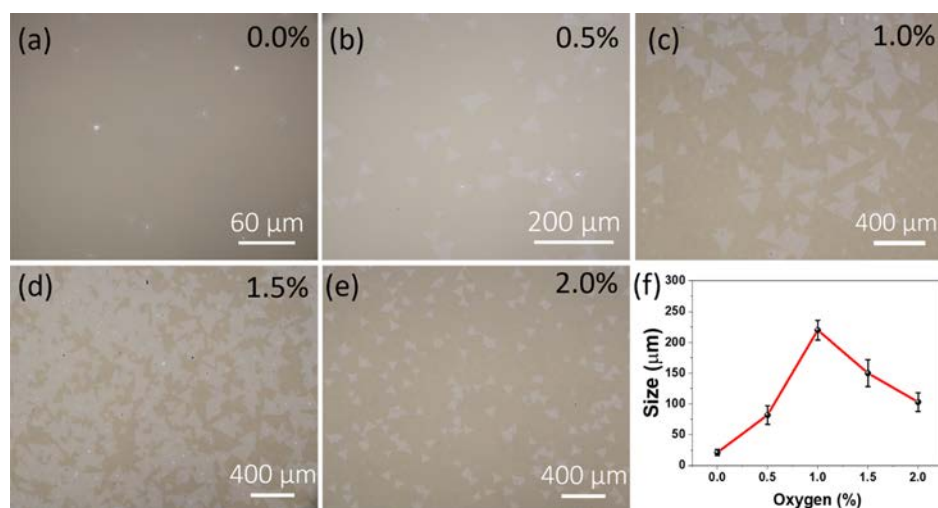
Figure 4. Morphology evolution of WS$_2$ as a function of oxygen concentration (in volume ratio) with a fixed reaction time of 20 min. (a) 0.0, (b) 0.5, (c) 1.0, (d) 1.5, and (e) 2.0%. (f) Average domain size as a function of oxygen ratio.

on the function of oxygen during this synthesis, the oxygen concentration manipulated in terms of volume ratio is varied for the material growth. Figure 4 illustrates the evolution of single-domain size of monolayer WS$_2$ as a function of oxygen concentration. Without feeding oxygen, only a few triangular-shaped WS$_2$ sheets are resulted, in which they have a relatively small lateral size of about 30 μm (Figure 4a), designating the importance of having oxygen species for large single-domain WS$_2$ films. According to reaction 1, there would not be any Na$_2$WO$_3$ formed without the introduction of oxygen. In this case, when no oxygen is intentionally fed, there is only residual oxygen left in the system that can react with NaOH to yield a tiny amount of Na$_2$WO$_3$. As a result, there is only a few WS$_2$ flakes found on the substrate. In contrast, with the feed of oxygen, for example, 0.5%, the size of WS$_2$ sheets is observed to become larger with an average size of around 80 μm (Figure 4b). When the oxygen concentration reaches 1.0%, the average size of the sheets increases to more than 210 μm (Figure 4c). However, the average sheet size decreases with further increasing the oxygen concentration (Figure 4d,e). The size evolution of WS$_2$ sheets is also shown in Figure 4f. Similarly, the crystal nucleation density of WS$_2$ can be roughly estimated from the number of triangular-shaped flakes. The estimated nucleation density as a function of oxygen concentration is then depicted in Supporting Information Figure S4. It is clear that the nucleation density slightly increases with the increasing oxygen content and then starts to decrease when the oxygen content hits 1.0%. For the further increase of oxygen concentration, the density of nuclei first increases and then reduces again. These results suggest that the growth of WS$_2$ sheets can be well controlled by manipulating the oxygen content during the material synthesis. By inspecting reaction 1, the oxygen concentration can be used to control the formation quantity of Na$_2$WO$_3$, which in turn dictates the gas concentration of WS$_2$ as described in reaction 2. The reduced size and nucleation density at high oxygen content can be attributed to the etching effect caused by oxygen as the following

$$O_2 + WS_2 \rightarrow WO_x + SO_y \qquad (3)$$

This way, the nucleation and growth of WS$_2$ can be effectively controlled by the above-discussed parameters;

therefore, a suitable amount of oxygen is required for the growth of large single-domain monolayer WS$_2$.

In addition to the effect of oxygen concentration, the growth duration also plays a key role in controlling the single-domain size of monolayer WS$_2$. As shown in Figure 5a, for the growth
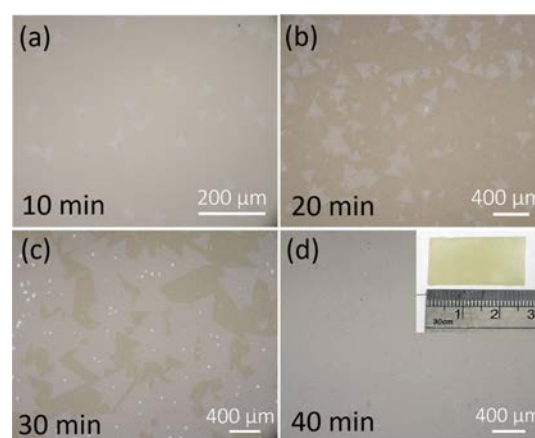

Figure 5. Morphology evolution of WS$_2$ as a function of growth time with fixed O$_2$ concentration of 1.0%. (a) 10, (b) 20, (c) 30, and (d) 40 min. Inset: Digital photograph of the sample with 40 min reaction time.

time of 10 min, the flakes are relatively small with a lateral size of around 30 μm. When the growth duration increases to 20 min, the lateral size of the flakes becomes much larger to about 200 μm (Figure 5b). With the growth time further increasing to 30 min, the flakes increase to a lateral size of 300−550 μm, while some of the flakes already join together (Figure 5c). Once the growth duration hits 40 min, almost all the flakes coalesce together, forming a continuous film (Figure 5d). A typical digital photograph of a continuous film of about 1.2 × 2.6 cm^2 is depicted in the Figure 5d inset, which indicates that large-area single-layer WS$_2$ films with large single domains can be readily obtained by the modified CVD method. The estimated nucleation density is also evaluated as a function of time (Supporting Information Figure S5). It is clear that the nucleation density monotonically decreases for the increasing growth time. The small flakes would vanish, while the large

flakes grow continuously. This reduced density of nuclei and increased size of the grains designate that the growth of these triangular-shaped WS_2 flakes follows the mechanism of Ostwald ripening or Smoluchowski ripening.[35] Evidently, these uniform and large single-domain monolayer WS_2 films can be effectively obtained with the optimized oxygen concentration as well as the long enough growth time.

For practical utilizations, it is essential to assess the electrical properties of these large single-domain monolayer WS_2. Here, global backgated FETs are constructed using the monolayer WS_2 as the device channel (Figure 6a inset). As depicted in the
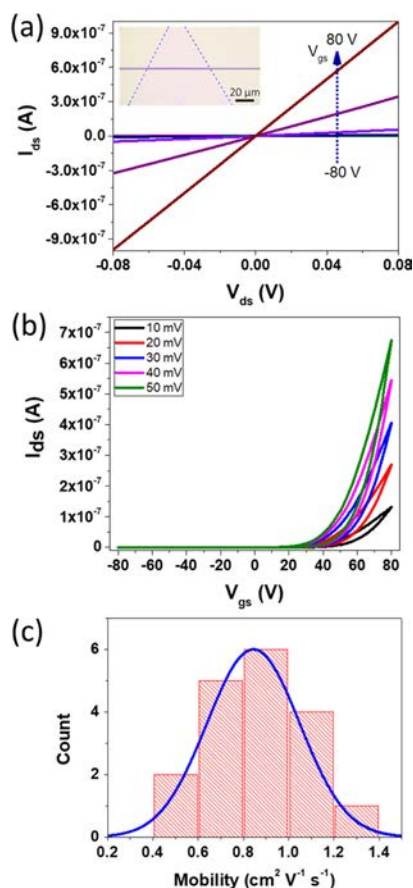

Figure 6. Electrical properties of the obtained triangular-shaped WS_2 flakes. (a) Output curves with different V_{gs}. The inset shows the optical microscope image of the fabricated device. (b) Transfer curves with different V_{ds}. (c) Statistical distribution of the extracted field-effect electron mobility.

device output curves in Figure 6a, the drain−source current, I_{ds}, increases with the increasing gate voltage V_{gs}, indicating the typical n-type conductivity of WS_2. The almost linear I_{ds}−V_{ds} curves suggest the Ohm-like contact between the electrodes and the WS_2 channel. At the same time, when the device transfer characteristics are assessed in Figure 6b, the I_{ds} increases with the increasing V_{gs}, which is consistent with the output curves. Based on the output curves, it can be inferred that the device operates in the linear regime. This way, the field-effect electron mobility of the channel can be extracted by the following equation of

$$\mu = \frac{\partial I_{ds}}{\partial V_{gs}} \cdot \frac{L}{W} \cdot \frac{1}{C_{ox} V_{ds}} \qquad (4)$$

where L is the channel length ($2\ \mu m$), W is the channel width ($73\ \mu m$), and C_{ox} is the gate capacitance per unit area ($1.27 \times 10^{-4}\ F\ m^{-2}$ for 270 nm thick SiO_2). In this case, the mobility is calculated to be $1.03\ cm^2\ V^{-1}\ s^{-1}$ for the device demonstrated in Figure 6a. The transistor gives a current ON/OFF ratio of about 10^7 as shown in the log-plot of the transfer curves in Supporting Information Figure S6. More devices are also measured with the mobility distribution compiled in Figure 6c. These monolayer WS_2 devices are observed to have a mobility in the range between 0.43 and $1.21\ cm^2\ V^{-1}\ s^{-1}$ with a center value of $0.84\ cm^2\ V^{-1}\ s^{-1}$, being well fitted by Gaussian function. These mobility values are already comparable with the ones of CVD-synthesized monolayer WS_2 reported in the literature (Table 1) and mechanically exfoliated monolayer WS_2.[36,37] Further improvement of the mobility can be easily realized by carefully tuning the growth parameters, using the high-k dielectrics,[38] and appropriate metal electrode[37] for the device fabrication.

Besides transistors, WS_2 is also an ideal active material for many optoelectronic devices. In this case, the photodetection performance of these large single-domain monolayer WS_2 films is as well evaluated. Figure 7a displays the I_{ds}−V_{ds} curves of the device with and without light irradiation. It is clear that the current increases with the increasing light intensity, demonstrating the photosensitive characteristics. In order to assess the performance of fabricated detectors, the photocurrent (I_p) as a function of light intensity (Φ) is measured as given in Figure 7b. Obviously, the photocurrent is observed to increase with the increasing light intensity, which is perfectly consistent with the I_{ds}−V_{ds} curves discussed above. The relationship between the photocurrent and the light intensity can be well modeled by an analytical equation of

$$I_p = A\Phi^{\alpha} \qquad (5)$$

where A and α are fitting parameters. By fitting the measured data, α is found to be 0.89. This sublinear relationship of the photocurrent with respect to the light intensity is mainly caused by the complex generation, trapping, and recombination processes of the photogenerated carriers, which are always witnessed in the low dimensional material-based photodetectors.[39−41] Here, as the α value is close to 1, it indicates a relatively low density of charge traps existing in WS_2. Furthermore, responsivity (R) is another figure of merit evaluating the capability of transforming light into current of a photodetector, which is defined as follows

$$R = \frac{I_p}{\Phi S} \qquad (6)$$

where S is the sensitive area of the photodetector ($440\ \mu m^2$). Based on the equation, the responsivity is compiled as a function of light intensity as shown in Figure 7b. At the same time, because R is also proportional to $\Phi^{1-\alpha}$ according to the eqs 5 and 6, it suggests that R would decrease with the increasing light intensity. This way, there is a maximum responsivity of $3.2\ mA\ W^{-1}$ observed when the light intensity is $0.03\ mW\ cm^{-2}$. With the increasing light intensity, the responsivity would reach a saturation value of $1.6\ mA\ W^{-1}$. This relatively high responsivity of the photodetector at low light intensity is caused by existence of charge traps here. At low light intensity, one kind of carriers, for example, if holes are trapped, the recombination rate of electrons and holes is reduced, leading to the increase of the lifetime, τ, of electrons.
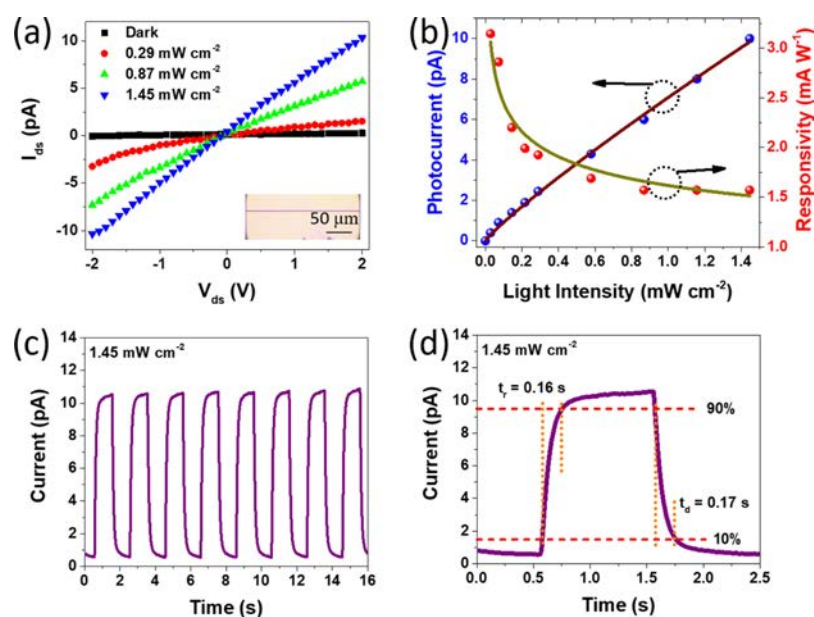
Figure 7. Photodetection performance of the obtained triangular-shaped WS_2 flakes. (a) $I_{ds}-V_{ds}$ curves under different light intensity. The inset shows the optical microscope image of the fabricated photodetector. (b) Photocurrent and responsivity vs light intensity. (c) Output current vs time under modulated light irradiation with a light intensity of 1.45 mW cm^{-2}. (d) High-resolution current versus time curve. The V_{ds} for (b–d) is 2 V. The wavelength of the light irradiation is 532 nm.

The gain, G, of a photoconductive detector is defined as $G = \tau/t_{tr}$ (t_{tr} is the transit time of carriers between electrodes). In this regard, the gain would increase at low light intensity, leading to the increase of responsivity. At high light intensity, most of the traps are filled, and the recombination rate of electrons and holes increases; therefore, the responsivity reduces accordingly. On the other hand, the operation stability of a photodetector under modulated light irradiation is extremely important for practical applications. As illustrated in Figure 7c, the stable on- and off-state current under modulated light irradiation are witnessed, confirming the excellent stability of the device. To get the corresponding response time of the photodetector, the high-resolution current versus time curve is collected and shown in Figure 7d. The rise (t_r) and decay (t_d) time are defined as the time interval for photocurrent varied from 10 to 90% and vise visa, respectively. In this case, the rise and decay time are determined to be 0.16 and 0.17 s, accordingly. These respectable photodetection characteristics clearly indicate the potential of these large single-domain monolayer WS_2 for high-performance optoelectronic devices.

CONCLUSIONS

In summary, ultralarge single-domain monolayer WS_2 films are successfully synthesized by the modified CVD method. These high-quality triangular-shaped WS_2 layers are characterized by TEM, optical spectroscopies and other techniques in details. It is found that the optimal introduction of a NaOH promoter is extremely important to achieve these large single domains of WS_2. The domain size can be well controlled by changing the oxygen concentration, growth duration, and other parameters. Importantly, when configured into global backgated transistors, they demonstrate a peak electron mobility up to 1.21 cm^2 V^{-1} s^{-1}, being comparable to other state-of-the-art WS_2 devices. Photodetectors based on these monolayer WS_2 also exhibit decent performance with a maximum responsivity of 3.2 mA W^{-1}. All these results evidently indicate that the modified CVD method here does not only provide a facile platform for the synthesis of high-quality, uniform, and large single-domain monolayer WS_2 films, but also facilitates their excellent intrinsic material properties for promising applications in next-generation electronics and optoelectronics.

ASSOCIATED CONTENT

Ⓢ Supporting Information

The Supporting Information is available free of charge on the ACS Publications website at DOI: 10.1021/acsami.9b12516.

> SEM image of a typical monolayer WS_2 triangle; WS_2 flake orientation relative to sapphire substrate; SEM image of W foil after reaction with and without NaOH; nucleation density of WS_2 versus oxygen concentration; nucleation density of monolayer WS_2 versus growth time; log-plot of the transfer curves (PDF)

AUTHOR INFORMATION

Corresponding Author
*E-mail: johnnyho@cityu.edu.hk.

ORCID Ⓡ
Changyong Lan: 0000-0002-5654-1098
Renjie Wei: 0000-0002-0459-7196
Johnny C. Ho: 0000-0003-3000-8794

Author Contributions

The manuscript was written through contributions of all authors. All authors have given approval to the final version of the manuscript.

Notes

The authors declare no competing financial interest.

ACKNOWLEDGMENTS

■ REFERENCES

(1) Manzeli, S.; Ovchinnikov, D.; Pasquier, D.; Yazyev, O. V.; Kis, A. 2D Transition Metal Dichalcogenides. *Nat. Rev. Mater.* **2017**, *2*, 17033.

(2) Sangwan, V. K.; Hersam, M. C. Electronic Transport in Two-Dimensional Materials. *Annu. Rev. Phys. Chem.* **2018**, *69*, 299–325.

(3) Shang, J.; Cong, C.; Wu, L.; Huang, W.; Yu, T. Light Sources and Photodetectors Enabled by 2D Semiconductors. *Small Methods* **2018**, *2*, 1800019.

(4) Li, H.; Wang, X.; Zhu, X.; Duan, X.; Pan, A. Composition Modulation in One-Dimensional and Two-Dimensional Chalcogenide Semiconductor Nanostructures. *Chem. Soc. Rev.* **2018**, *47*, 7504–7521.

(5) Luo, P.; Zhuge, F.; Zhang, Q.; Chen, Y.; Lv, L.; Huang, Y.; Li, H.; Zhai, T. Doping Engineering and Functionalization of Two-Dimensional Metal Chalcogenides. *Nanoscale Horiz.* **2019**, *4*, 26–51.

(6) Cong, C.; Shang, J.; Wang, Y.; Yu, T. Optical Properties of 2D Semiconductor WS_2. *Adv. Opt. Mater.* **2018**, *6*, 1700767.

(7) Lan, C.; Li, C.; Yin, Y.; Liu, Y. Large-Area Synthesis of Monolayer WS_2 and Its Ambient-Sensitive Photo-Detecting Performance. *Nanoscale* **2015**, *7*, 5974–5980.

(8) Lan, C.; Zhou, Z.; Zhou, Z.; Li, C.; Shu, L.; Shen, L.; Li, D.; Dong, R.; Yip, S.; Ho, J. C. Wafer-Scale Synthesis of Monolayer WS_2 for High-Performance Flexible Photodetectors by Enhanced Chemical Vapor Deposition. *Nano Res.* **2018**, *11*, 3371–3384.

(9) Yang, W.; Shang, J.; Wang, J.; Shen, X.; Cao, B.; Peimyoo, N.; Zou, C.; Chen, Y.; Wang, Y.; Cong, C.; Huang, W.; Yu, T. Electrically Tunable Valley-Light Emitting Diode (vLED) Based on CVD-Grown Monolayer WS_2. *Nano Lett.* **2016**, *16*, 1560–1567.

(10) Choi, W.; Choudhary, N.; Han, G. H.; Park, J.; Akinwande, D.; Lee, Y. H. Recent Development of Two-Dimensional Transition Metal Dichalcogenides and Their Applications. *Mater. Today* **2017**, *20*, 116–130.

(11) Lai, J.; Liu, X.; Ma, J.; Wang, Q.; Zhang, K.; Ren, X.; Liu, Y.; Gu, Q.; Zhuo, X.; Lu, W.; Wu, Y.; Li, Y.; Feng, J.; Zhou, S.; Chen, J.-H.; Sun, D. Anisotropic Broadband Photoresponse of Layered Type-II Weyl Semimetal $MoTe_2$. *Adv. Mater.* **2018**, *30*, 1707152.

(12) Wu, J.; Wang, J.; Pan, D.; Li, Y.; Jiang, C.; Li, Y.; Jin, C.; Wang, K.; Song, F.; Wang, G.; Zhang, H.; Wan, J. Synchronous Growth of High-Quality Bilayer Bernal Graphene: From Hexagonal Single-Crystal Domains to Wafer-Scale Homogeneous Films. *Adv. Funct. Mater.* **2017**, *27*, 1605927.

(13) Yu, Y.; Li, C.; Liu, Y.; Su, L.; Zhang, Y.; Cao, L. Controlled Scalable Synthesis of Uniform, High-Quality Monolayer and Few-Layer MoS_2 Films. *Sci. Rep.* **2013**, *3*, 1866.

(14) Xu, Z.-Q.; Zhang, Y.; Lin, S.; Zheng, C.; Zhong, Y. L.; Xia, X.; Li, Z.; Sophia, P. J.; Fuhrer, M. S.; Cheng, Y.-B.; Bao, Q. Synthesis and Transfer of Large-Area Monolayer WS_2 Crystals: Moving Toward the Recyclable Use of Sapphire Substrates. *ACS Nano* **2015**, *9*, 6178–6187.

(15) Chen, Y.; Gan, L.; Li, H.; Ma, Y.; Zhai, T. Achieving Uniform Monolayer Transition Metal Dichalcogenides Film on Silicon Wafer via Silanization Treatment: A Typical Study on WS_2. *Adv. Mater.* **2017**, *29*, 1603550.

(16) Yue, Y.; Chen, J.; Zhang, Y.; Ding, S.; Zhao, F.; Wang, Y.; Zhang, D.; Li, R.; Dong, H.; Hu, W.; Feng, Y.; Feng, W. Two-Dimensional High-Quality Monolayered Triangular WS_2 Flakes for Field-Effect Transistors. *ACS Appl. Mater. Interfaces* **2018**, *10*, 22435–22444.

(17) Gao, Y.; Liu, Z.; Sun, D.-M.; Huang, L.; Ma, L.-P.; Yin, L.-C.; Ma, T.; Zhang, Z.; Ma, X.-L.; Peng, L.-M.; Cheng, H.-M.; Ren, W. Large-Area Synthesis of High-Quality and Uniform Monolayer WS_2 on Reusable Au Foils. *Nat. Commun.* **2015**, *6*, 8569.

(18) Yang, P.; Zou, X.; Zhang, Z.; Hong, M.; Shi, J.; Chen, S.; Shu, J.; Zhao, L.; Jiang, S.; Zhou, X.; Huan, Y.; Xie, C.; Gao, P.; Chen, Q.; Zhang, Q.; Liu, Z.; Zhang, Y. Batch Production of 6-Inch Uniform Monolayer Molybdenum Disulfide Catalyzed by Sodium in Glass. *Nat. Commun.* **2018**, *9*, 979.

(19) Lan, C.; Li, D.; Zhou, Z.; Yip, S.; Zhang, H.; Shu, L.; Wei, R.; Dong, R.; Ho, J. C. Direct Visualization of Grain Boundaries in 2D Monolayer WS_2 via Induced Growth of CdS Nanoparticle Chains. *Small Methods* **2019**, *3*, 1800245.

(20) Zhang, Y.; Zhang, Y.; Ji, Q.; Ju, J.; Yuan, H.; Shi, J.; Gao, T.; Ma, D.; Liu, M.; Chen, Y.; Song, X.; Hwang, H. Y.; Cui, Y.; Liu, Z. Controlled Growth of High-Quality Monolayer WS_2 Layers on Sapphire and Imaging Its Grain Boundary. *ACS Nano* **2013**, *7*, 8963–8971.

(21) Nie, Y.; Liang, C.; Zhang, K.; Zhao, R.; Eichfeld, S. M.; Cha, P.-R.; Colombo, L.; Robinson, J. A.; Wallace, R. M.; Cho, K. First Principles Kinetic Monte Carlo Study on the Growth Patterns of WSe_2 Monolayer. *2D Mater.* **2016**, *3*, 025029.

(22) Dumcenco, D.; Ovchinnikov, D.; Marinov, K.; Lazić, P.; Gibertini, M.; Marzari, N.; Sanchez, O. L.; Kung, Y.-C.; Krasnozhon, D.; Chen, M.-W.; Bertolazzi, S.; Gillet, P.; Fontcuberta i Morral, A.; Radenovic, A.; Kis, A. Large-Area Epitaxial Monolayer MoS2. *ACS Nano* **2015**, *9*, 4611–4620.

(23) Yu, H.; Liao, M.; Zhao, W.; Liu, G.; Zhou, X. J.; Wei, Z.; Xu, X.; Liu, K.; Hu, Z.; Deng, K.; Zhou, S.; Shi, J.-A.; Gu, L.; Shen, C.; Zhang, T.; Du, L.; Xie, L.; Zhu, J.; Chen, W.; Yang, R.; Shi, D.; Zhang, G. Wafer-Scale Growth and Transfer of Highly-Oriented Monolayer MoS_2 Continuous Films. *ACS Nano* **2017**, *11*, 12001–12007.

(24) Ji, Q.; Kan, M.; Zhang, Y.; Guo, Y.; Ma, D.; Shi, J.; Sun, Q.; Chen, Q.; Zhang, Y.; Liu, Z. Unravelling Orientation Distribution and Merging Behavior of Monolayer MoS_2 Domains on Sapphire. *Nano Lett.* **2014**, *15*, 198–205.

(25) Yun, S. J.; Chae, S. H.; Kim, H.; Park, J. C.; Park, J.-H.; Han, G. H.; Lee, J. S.; Kim, S. M.; Oh, H. M.; Seok, J.; Jeong, M. S.; Kim, K. K.; Lee, Y. H. Synthesis of Centimeter-Scale Monolayer Tungsten Disulfide Film on Gold Foils. *ACS Nano* **2015**, *9*, 5510–5519.

(26) Rong, Y.; Fan, Y.; Leen Koh, A.; Robertson, A. W.; He, K.; Wang, S.; Tan, H.; Sinclair, R.; Warner, J. H. Controlling Sulphur Precursor Addition for Large Single Crystal Domains of WS_2. *Nanoscale* **2014**, *6*, 12096–12103.

(27) Cong, C.; Shang, J.; Wu, X.; Cao, B.; Peimyoo, N.; Qiu, C.; Sun, L.; Yu, T. Synthesis and Optical Properties of Large-Area Single-Crystalline 2D Semiconductor WS_2 Monolayer from Chemical Vapor Deposition. *Adv. Opt. Mater.* **2014**, *2*, 131–136.

(28) Sheng, Y.; Tan, H.; Wang, X.; Warner, J. H. Hydrogen Addition for Centimeter-Sized Monolayer Tungsten Disulfide Continuous Films by Ambient Pressure Chemical Vapor Deposition. *Chem. Mater.* **2017**, *29*, 4904–4911.

(29) Xue, H.; Wang, Y.; Dai, Y.; Kim, W.; Jussila, H.; Qi, M.; Susoma, J.; Ren, Z.; Dai, Q.; Zhao, J.; Halonen, K.; Lipsanen, H.; Wang, X.; Gan, X.; Sun, Z. A $MoSe_2/WSe_2$ Heterojunction-Based Photodetector at Telecommunication Wavelengths. *Adv. Funct. Mater.* **2018**, *28*, 1804388.

(30) Li, C.; Yamaguchi, Y.; Kaneko, T.; Kato, T. Large Single-Domain Growth of Monolayer WS_2 by Rapid-Cooling Chemical Vapor Deposition. *Appl. Phys. Express* **2017**, *10*, 075201.

(31) Reale, F.; Palczynski, P.; Amit, I.; Jones, G. F.; Mehew, J. D.; Bacon, A.; Ni, N.; Sherrell, P. C.; Agnoli, S.; Craciun, M. F.; Russo, S.; Mattevi, C. High-Mobility and High-Optical Quality Atomically Thin WS_2. *Sci. Rep.* **2017**, *7*, 14911.

(32) Zhao, W.; Ghorannevis, Z.; Amara, K. K.; Pang, J. R.; Toh, M.; Zhang, X.; Kloc, C.; Tan, P. H.; Eda, G. Lattice Dynamics in Mono- and Few-Layer Sheets of WS_2 and WSe_2. *Nanoscale* **2013**, *5*, 9677–9683.

(33) Gutiérrez, H. R.; Perea-López, N.; Elías, A. L.; Berkdemir, A.; Wang, B.; Lv, R.; López-Urías, F.; Crespi, V. H.; Terrones, H.; Terrones, M. Extraordinary Room-Temperature Photoluminescence in Triangular WS_2 Monolayers. *Nano Lett.* **2013**, *13*, 3447−3454.

(34) Chow, P. K.; Jacobs-Gedrim, R. B.; Gao, J.; Lu, T.-M.; Yu, B.; Terrones, H.; Koratkar, N. Defect-Induced Photoluminescence in Monolayer Semiconducting Transition Metal Dichalcogenides. *ACS Nano* **2015**, *9*, 1520−1527.

(35) Zhang, X.; Choudhury, T. H.; Chubarov, M.; Xiang, Y.; Jariwala, B.; Zhang, F.; Alem, N.; Wang, G.-C.; Robinson, J. A.; Redwing, J. M. Diffusion-Controlled Epitaxy of Large Area Coalesced WSe_2 Monolayers on Sapphire. *Nano Lett.* **2018**, *18*, 1049−1056.

(36) Ovchinnikov, D.; Allain, A.; Huang, Y.-S.; Dumcenco, D.; Kis, A. Electrical Transport Properties of Single-Layer WS_2. *ACS Nano* **2014**, *8*, 8174−8181.

(37) Wang, Y.; Kim, J. C.; Wu, R. J.; Martinez, J.; Song, X.; Yang, J.; Zhao, F.; Mkhoyan, A.; Jeong, H. Y.; Chhowalla, M. Van der Waals Contacts between Three-Dimensional Metals and Two-Dimensional Semiconductors. *Nature* **2019**, *568*, 70−74.

(38) Cui, Y.; Xin, R.; Yu, Z.; Pan, Y.; Ong, Z.-Y.; Wei, X.; Wang, J.; Nan, H.; Ni, Z.; Wu, Y.; Chen, T.; Shi, Y.; Wang, B.; Zhang, G.; Zhang, Y.-W.; Wang, X. High-Performance Monolayer WS_2 Field-Effect Transistors on High-k Dielectrics. *Adv. Mater.* **2015**, *27*, 5230−5234.

(39) Lan, C.; Li, C.; Wang, S.; He, T.; Zhou, Z.; Wei, D.; Guo, H.; Yang, H.; Liu, Y. Highly Responsive and Broadband Photodetectors Based on WS_2-Graphene van der Waals Epitaxial Heterostructures. *J. Mater. Chem. C* **2017**, *5*, 1494−1500.

(40) Lan, C.; Dong, R.; Zhou, Z.; Shu, L.; Li, D.; Yip, S.; Ho, J. C. Large-Scale Synthesis of Freestanding Layer-Structured PbI_2 and $MAPbI_3$ Nanosheets for High-Performance Photodetection. *Adv. Mater.* **2017**, *29*, 1702759.

(41) Lan, C.; Li, C.; Yin, Y.; Guo, H.; Wang, S. Synthesis of Single-Crystalline GeS Nanoribbons for High Sensitivity Visible-Light Photodetectors. *J. Mater. Chem. C* **2015**, *3*, 8074−8079.